
# Role of Nonequilibrium Populations in Dark-Exciton Formation

# Role of Nonequilibrium Populations in Dark-Exciton Formation

Paul Werner,[1] Wiebke Bennecke,[1] Jan Philipp Bange,[1] Giuseppe Meneghini,[2,3] David Schmitt,[1] Marco Merboldt,[1] Anna M. Seiler,[1] AbdulAziz AlMutairi,[4,5] Kenji Watanabe,[6] Takashi Taniguchi,[7] G. S. Matthijs Jansen,[1] Junde Liu,[1] Daniel Steil,[1] Stephan Hofmann,[4] R. Thomas Weitz,[1,8] Ermin Malic,[2,3,9] Stefan Mathias,[1,8,*] and Marcel Reutzel[1,2,3,†]

[1]*I. Physikalisches Institut, Georg-August-Universität Göttingen, Friedrich-Hund-Platz 1, 37077 Göttingen, Germany*
[2]*Fachbereich Physik, Philipps-Universität Marburg, 35032 Marburg, Germany*
[3]*mar.quest—Marburg Center for Quantum Materials and Sustainable Technologies, 35032 Marburg, Germany*
[4]*Department of Engineering, University of Cambridge, Cambridge CB3 0FA, United Kingdom*
[5]*King Fahd University of Petroleum and Minerals (KFUPM), Dhahran, Saudi Arabia*
[6]*Research Center for Electronic and Optical Materials, National Institute for Materials Science, 1-1 Namiki, Tsukuba 305-0044, Japan*
[7]*Research Center for Materials Nanoarchitectonics, National Institute for Materials Science, 1-1 Namiki, Tsukuba 305-0044, Japan*
[8]*International Center for Advanced Studies of Energy Conversion (ICASEC), University of Göttingen, Göttingen, Germany*
[9]*Department of Physics, Chalmers University of Technology, Gothenburg, Sweden*

(Received 17 June 2025; accepted 25 March 2026; published 8 May 2026)

The optical excitation of a bright exciton may be followed by the formation of lower-energy dark states. In these formation and relaxation processes, nonequilibrium exciton and phonon populations play a dominant role but remain so far largely unexplored, as most states are inaccessible by regular spectroscopies. Here, on the example of homobilayer 2H-$MoS_2$, we realize direct access to the full exciton relaxation cascade from experiment and theory. We find distinct changes in the time-, energy-, and in-plane momentum-resolved photoemission spectral function that can be explained only when considering the formation and subsequent thermalization of excitonic nonequilibrium occupation distributions. In agreement with microscopic many-particle calculations, we quantify the timescales for the formation of a nonequilibrium dark-excitonic occupation and its subsequent thermalization to 85 and 150 fs, respectively. Our results provide a previously inaccessible view of the complete exciton relaxation cascade, which is of importance for the future characterization of nonequilibrium excitonic phases and the efficient design of optoelectronic devices.

DOI: 10.1103/w29j-z48v

Transition metal dichalcogenides have become a promising platform for the next-generation optoelectronic devices [1,2]. This is because the energy landscape of excitations is built up by excitons [3,4], whose energy $E_{\mathrm{exc}}$, kinetic center-of-mass momentum $\boldsymbol{Q}$, and dynamics can be controlled via multiple parameters such as interlayer hybridization [5,6], charge-carrier density [7], dielectric environment [8], moiré potential [9–11], or the proximity of correlated phases [12]. Concerning the exciton formation and thermalization dynamics [13], Fig. 1(a) illustrates how scattering processes can lead to the buildup of strong nonequilibrium (NEQ) exciton populations: After optical excitation of bright exciton states within the light cone ($\boldsymbol{Q} \approx 0$), exciton-phonon, exciton-exciton, and exchange-driven scattering events can lead to a redistribution of the energy- and $\boldsymbol{Q}$-momentum-dependent $E^{i}_{\mathrm{exc}}(\boldsymbol{Q})$ exciton population within the same exciton parabola ($i = KK$) and toward energetically favorable dark excitons that can be of momentum-indirect or spin-forbidden nature ($i = \Gamma K, \Gamma\Sigma$) [14–21]. Given the stark energy difference between the quasiparticles involved in the scattering processes, such as excitons at electron-volt scales versus phonons at millielectron-volt scales, the resulting exciton and phonon populations after scattering must occupy NEQ states and distributions ($\boldsymbol{Q} \neq 0$) [22,23]. Additional energy dissipation processes are necessary for the exciton population to thermalize toward $\boldsymbol{Q} \approx 0$. Depending on the energetic alignment of the excitonic states and the available phonon modes, this thermalization process can take a few femto- to picoseconds. Therefore, to understand and tailor the excitonic formation and thermalization processes, an understanding of initial NEQ exciton dynamics is necessary.

While microscopic model calculations naturally capture the $E^{i}_{\mathrm{exc}}(\boldsymbol{Q})$-resolved exciton dynamics [17,24], experimental access is challenging. This is because all-optical spectroscopies are typically sensitive to only transitions

*Contact author: smathias@uni-goettingen.de
†Contact author: marcel.reutzel@uni-marburg.de

within the light cone and are limited with regard to $\boldsymbol{Q}$-momentum-resolved experiments [13]. Still, selected all-optical spectroscopies [18,25–27] could differentiate the respective timescales of formation and thermalization, e.g., by evaluating phonon-assisted secondary [26] or internal $1s$-$2p$ [18,27] transitions. Complementary, time- and angle-resolved photoemission spectroscopy (trARPES) provides access to the full momentum-space distribution and is ideally suited to resolve the $E^{i}_{\mathrm{exc}}(\boldsymbol{Q})$-resolved exciton dynamics [28]. Recent trARPES experiments enabled the direct experimental access to dark excitons whose wave function is composed of valence and conduction band states with different valley indices [19–21,29–36]. However, probing the energy- and $\boldsymbol{Q}$-momentum-resolved dynamics is a more challenging scenario, because the photoemission experiment is not sensitive to the exciton center-of-mass momentum $\boldsymbol{Q}$ but to the in-plane momentum $\boldsymbol{k}_{\parallel}$ of the single-particle electrons that result from the breakup of excitons in the photoemission process. Hence, even though there are theoretical predictions on how $\boldsymbol{Q}$-momentum-dependent exciton populations would appear in the $E(\boldsymbol{k}_{\parallel})$-resolved experiment [24,37–41], it has not yet been shown that trARPES can address the $E^{i}_{\mathrm{exc}}(\boldsymbol{Q})$-dependent dynamics of excitons.

Here, we demonstrate the contribution of NEQ excitonic occupations to formation and thermalization processes from experiment and theory. We chose homobilayer (BL) 2H-$MoS_2$ as our model system. This material is perfectly suited to create and study NEQ exciton populations, because its dark-exciton landscape necessitates the creation of NEQ exciton distributions following an optical excitation [Figs. 1(a) and 1(b)] [24,42,43]. We follow the ultrafast scattering processes in experiment using

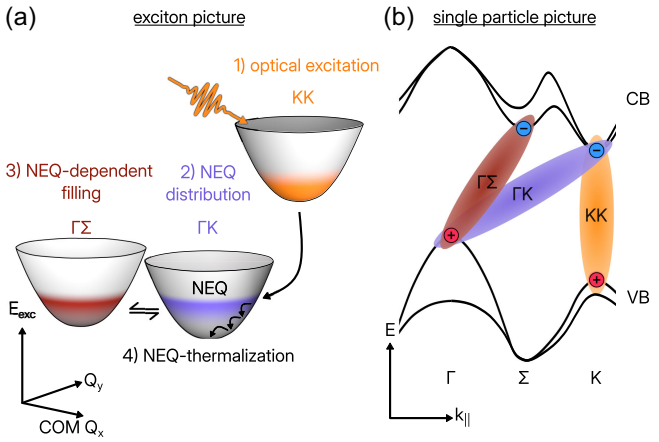


FIG. 1. Formation and thermalization of nonequilibrium excitonic occupations. (a) Low-energy landscape of excitons in homobilayer 2H-$MoS_2$ and optically induced quasiparticle NEQ scattering dynamics. (b) Single-particle energy landscape, where the $KK$ (orange), $\Gamma K$ (violet), and $\Gamma\Sigma$ (brown) excitons are composed of single-particle Bloch states originating from the 2H-$MoS_2$ valence and conduction bands.

time-resolved photoemission momentum microscopy [44,45] and are able to get a clear contribution of NEQ excitons to the observed exciton dynamics. Specifically, we find a time-dependent broadening and narrowing of the $\boldsymbol{k}_{\parallel}$-momentum width of the excitonic photoemission signatures, which are indicative for the formation and thermalization of NEQ dark-excitonic occupations. Our data are supported by microscopic many-particle calculations based on density matrix formalism [31,46]. We find that the NEQ distribution in BL 2H-$MoS_2$ is formed with a rise time of ≈85 fs and thermalizes with a time constant of ≈150 fs. Our Letter opens the door to study NEQ exciton occupations and their role in the formation and thermalization dynamics in arbitrary two-dimensional semiconductors such as $WSe_2$, $MoS_2$, and their heterostructures. More broadly, this identification of NEQ signatures in trARPES can facilitate the future study of NEQ excitonic phases in quantum materials and support the development of van der Waals semiconductor devices.

*The exciton energy landscape of homobilayer 2H-$MoS_2$*—Figures 1(a) and 1(b) illustrate the low-energy landscape of excitons in BL 2H-$MoS_2$ in the exciton and the single-particle picture, consisting of the optically bright $A1s$ exciton and two additional momentum-indirect dark excitons. We label the $A1s$ exciton as "$KK$," because the exciton's hole and electron components reside in the $K$-valley valence and conduction bands, respectively [Fig. 1(b)]. In the same notation, the two energetically relevant momentum-indirect dark excitons are labeled as $\Gamma K$ and $\Gamma\Sigma$ excitons. Because we consider only an excitation resonant to the $KK$ exciton energy, we can exclude the contribution of higher-energy excitations such as the $B$ exciton and interlayer $KK'$ excitons [24,47,48]. Moreover, the contribution of spin-dark excitons is excluded, because they are formed only on a much longer timescale [49,50]. In this energy landscape, it can then be anticipated that the population of the optically excited $KK$ excitons decays via intervalley hole transfer (black arrow) in an exciton-phonon scattering process to the energetically favorable $\Gamma K$ exciton [15]. Importantly, the energetic separation between the exciton band minima of the bright $KK$ and the dark $\Gamma K$ excitons in BL $MoS_2$ is ≈400 meV and, therefore, much larger than typical phonon energies of ≈30 meV [51]. Hence, exciton population transfer via exciton-phonon scattering from $KK$ to $\Gamma K$ must lead to a NEQ exciton distribution in the $\Gamma K$ state, i.e., creation of NEQ dark excitons with considerable excess energy [violet region in Fig. 1(a)]. It is this NEQ distribution and its subsequent thermalization toward $\boldsymbol{Q} \approx 0$ that we aim to probe with momentum microscopy.

Using time-resolved momentum microscopy ([44,45], details in End Matter), we identify the signatures of the different bright and dark excitons in the photoelectron spectra. Figure 2(a) shows an $E(\boldsymbol{k}_{\parallel})$-resolved spectrum taken at $\Delta t = -1000$ fs. We find the highest occupied

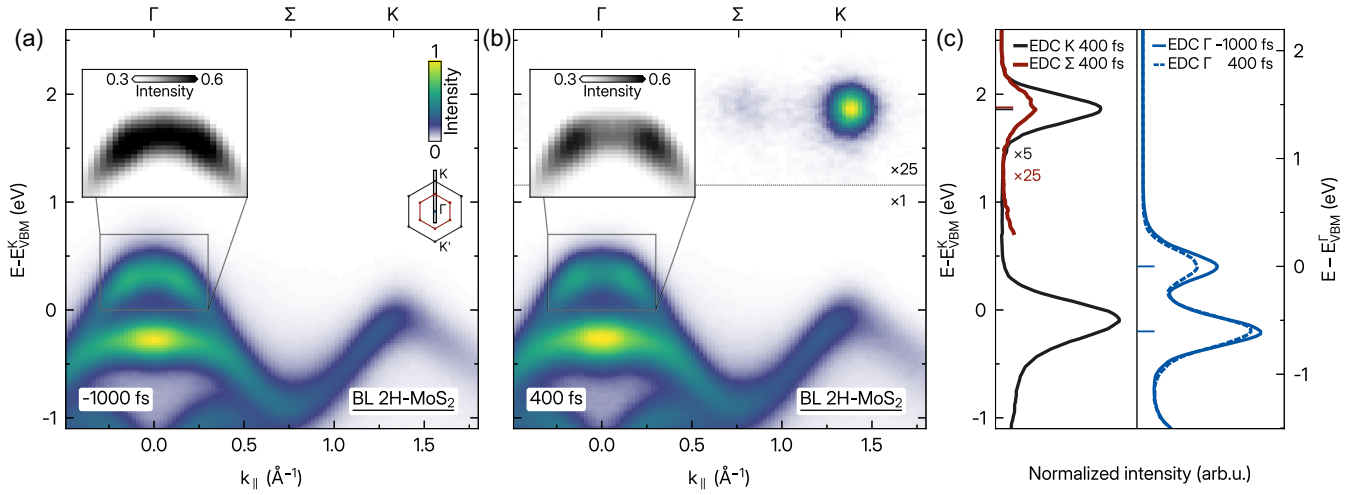


FIG. 2. Energy- and $\boldsymbol{k}_{\parallel}$-momentum-resolved photoemission spectra of BL 2H-$MoS_2$. (a),(b) In addition to the valence band structure at energies $E - E^K_{\mathrm{VBM}} < 0.5$ eV, spectral weight originating from the breakup of excitons is observed at the $K$ and the Σ valley for $E\text{-}E^K_{\mathrm{VBM}} > 1$ eV after optical excitation [(b) at 400 fs]. At 400 fs, a distinct suppression of intensity at the Γ-valley valence band maximum indicates the presence of excitonic holes in 2H-$MoS_2$ (cf. insets). (c) Energy-distribution curves integrated in a $0.09 \times 0.09$ Å$^{-2}$-wide momentum region around the $K$ valley (black), the Σ valley (brown), and the Γ valley (blue).

valence band at the Γ valley, where the double-peaked structure is indicative of the bilayer nature of the sample [42,52]. At $\Delta t = 400$ fs after resonant excitation of the bright $A1s$ excitons (1.9 eV) [Fig. 2(b)], we find additional spectral weight at (i) the $K$ valley and (ii) the Σ valley at higher energies, and (iii) a distinct suppression of spectral weight at the Γ-valley VBM. We can attribute these photoemission signatures to specific exciton species as follows: The $K$- and Σ-valley spectral weight result from the photoelectrons that did belong to excitons whose electron component resided in the respective $K$ and Σ valleys [19,20,28,29,31]. Hence, the $K$-valley spectral weight is indicative for the presence of $KK$ and/or Γ$K$ excitons. Similarly, the Σ-valley spectral weight results from the breakup of ΓΣ excitons. Intriguingly, the Γ$K$ and ΓΣ exciton's hole contributions can also directly be verified by the observation of missing valence band spectral weight at the VBM of the Γ valley [32]. For a quantitative description, we evaluate the energies of all contributing bright and dark excitons (see End Matter) [28,34,53], which are in excellent agreement with our *ab initio* calculated results and earlier photoluminescence experiments [42,43] (see Table I).

*Signatures of NEQ exciton occupations in the ultrafast dynamics*—We now consider the delay-resolved experiment to quantify population transfer between the excitonic states. Importantly, since the photoemission signatures of the $KK$ and Γ$K$ excitons coincide, we expect unusual dynamics for photoelectrons detected at the $K$ point. Figure 3(a) shows the delay-dependent total photoelectron intensity at the $K$ valley (black circles) and the Σ valley (red squares), which corresponds to the sum of the population dynamics of $KK$ and Γ$K$ excitons (signal at $K$) and ΓΣ excitons (signal at Σ). The signal at $K$ shows a pronounced dip around 100 fs and a delayed rise thereafter, which would not be expected for a simple cascaded population transfer. We propose that this dip can be understood only if a NEQ population transfer from Γ$K$ to ΓΣ excitons is considered: While the population at Γ$K$ is in a NEQ, excitons that transfer from Γ$K$ to ΓΣ do not contribute to spectral weight at the $K$ valley, leading to a transient reduction of the $K$-valley signal. Simultaneously, photoemission spectral weight at the Σ valley increases as ΓΣ exciton occupation is formed. At later times, the drop of Σ-valley spectral weight and the second rise at $K$ is caused by the backtransfer from ΓΣ to Γ$K$ due to thermalization of the NEQ distribution.

In order to support this proposition, we simulate the delay- and $E(\boldsymbol{Q})$-dependent population dynamics of $KK$, Γ$K$, and ΓΣ excitons with the exciton density matrix formalism [31,46] (see Supplemental Material [54]). The calculated $E(\boldsymbol{Q})$-momentum-integrated population dynamics is overlaid as lines on the experimental data in Fig. 3(a) (cf. Supplemental Material Fig. S1 [54]). Importantly, we find that the dip in the experimental $K$-valley dynamics is also present in our theoretical analysis, if we consider the joint occupation dynamics of both excitons that are probed at the $K$ valley [i.e., $KK$ and Γ$K$ excitons, solid black line in Fig. 3(a)].

For a more detailed understanding of the NEQ dynamics, Figs. 3(b)–3(e) show snapshots of the calculated $E(\boldsymbol{Q})$-resolved exciton populations. The first observation is that, subsequent to the optical excitation of bright $KK$ excitons, intravalley exciton-phonon scattering leads to a broadening of the $KK$ exciton population to $\boldsymbol{Q}$ momenta outside the light cone [Figs. 3(b) and 3(c)]. In addition, the emission of $K$ phonons and $M$ phonons (Σ phonons) enables intervalley

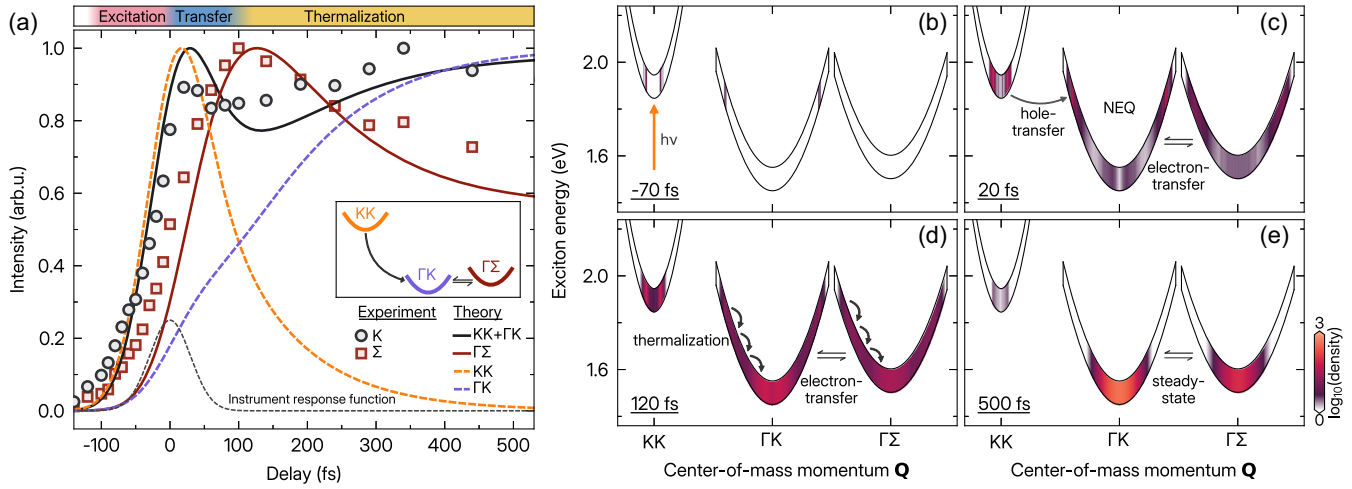


FIG. 3. Exciton formation and thermalization dynamics in homobilayer 2H-$MoS_2$. (a) Energy- and $\boldsymbol{k}_{\parallel}$-momentum-integrated excitonic photoemission spectral weight extracted at the $K$ valley (black circles) and the $\Sigma$ valley (red squares) as a function of delay together with microscopic model calculations that capture the NEQ population dynamics of $KK$ (orange), $\Gamma K$ (violet), and $\Gamma\Sigma$ (brown) excitons. Note that the $K$-valley ($\Sigma$-valley) spectral weight corresponds to the sum of the $KK$ and $\Gamma K$ populations (the $\Gamma\Sigma$ population). The inset illustrates the exciton scattering cascade $KK \rightarrow \Gamma K \rightleftharpoons \Gamma\Sigma$. (b)–(e) Delay-dependent snapshots of the calculated energy- and $\boldsymbol{Q}$-momentum-resolved exciton population dynamics for $KK$, $\Gamma K$, and $\Gamma\Sigma$ excitons subsequent to the resonant excitation of $KK$ excitons. Exciton-phonon scattering leads to the formation of a NEQ distribution of $KK$, $\Gamma K$, and $\Gamma\Sigma$ excitons (b), (c). Only subsequent intra- and intervalley scattering processes lead to the thermalization of the exciton population distribution and the establishment of a $\Gamma K \rightleftharpoons \Gamma\Sigma$ steady state (d), (e).

hole transfer processes that transfer $KK$ exciton population to $\Gamma K$ and intervalley electron transfer processes that transfer $\Gamma K$ exciton population to the $\Gamma\Sigma$ state, respectively [15]. Importantly, Fig. 3(c) shows that not only the initial $\Gamma K$, but also the $\Gamma\Sigma$ exciton population is clearly in a NEQ condition. At 120 fs, subsequent intra- and intervalley exciton-phonon scattering events have lead to the thermalization of the exciton populations and the formation of a $\Gamma K \rightleftharpoons \Gamma\Sigma$ steady state [Fig. 3(d)]. As the time delay increases, the major part of the exciton population becomes of $\Gamma K$ nature [Fig. 3(e)], because the $\Gamma K$ exciton state is energetically most favorable. In particular, we find that the dynamics can be grouped into the delay regimes of optical excitation [$-100$ fs $< \Delta t < 0$ fs, red $\Delta t$ regime in Fig. 3(a)], intervalley charge-transfer and dark-exciton formation (0 fs $< \Delta t <$ 100 fs, blue), and the thermalization of the exciton populations ($\Delta t >$ 100 fs, yellow).

*NEQ exciton dynamics probed in the photoemission spectral function*—To capture the NEQ dynamics and the distinctly different timescales for exciton formation and thermalization, it is necessary to differentiate $\boldsymbol{Q} \approx 0$ and $\boldsymbol{Q} \neq 0$ exciton momentum distributions in the $E(\boldsymbol{k}_{\parallel})$-resolved photoemission experiment. It is established that $\boldsymbol{Q} \approx 0$ excitons lead to holelike photoemission signatures mirroring the $\boldsymbol{k}_{\parallel}$-dependent valence band dispersion [29,30]. For thermal and NEQ $\boldsymbol{Q} \neq 0$ distributions, however, so far no experimental signatures have been discussed in detail. Rustagi and Kemper [39] predicted that NEQ distributions ($\boldsymbol{Q} \neq 0$) should lead to distinct deviations from the holelike dispersion, including a broadening of the photoemission spectral weight on the photoelectron energy- and $\boldsymbol{k}_{\parallel}$-momentum axis [33].

Guided by the clear experimental and theoretical results of NEQ dynamics, Figs. 4(a)–4(c) illustrate $E(\boldsymbol{k}_{\parallel})$-resolved photoemission snapshots collected at the $K$ valley. As this spectral weight has contributions from the breakup of $KK$ and $\Gamma K$ excitons, it is not possible to directly probe a signature of the ringlike $\boldsymbol{Q}$-dependent NEQ occupation for $\Gamma K$ excitons in the 60 fs data. Nevertheless, differences in the momentum-dependent dynamics are clearly identifiable, in particular, in the difference map shown in Fig. 4(d) and in the extracted momentum-filtered energy-distribution curves in Fig. 4(e).

To quantify the spectral changes systematically, Figs. 4(f) and 4(g) show the delay dependence of energy-integrated momentum-distribution curves (MDCs) of the exciton photoemission signatures at the $K$ and $\Sigma$ valley. On top of the color-coded photoemission yield, the lines indicate the full width at half maximum $\theta_i$ ($i = K, \Sigma$) obtained by Gaussian fits to the MDCs (End Matter). Moreover, the fit results $\theta_i$ are plotted as a function of delay in Fig. 4(h). First, for the $K$-valley spectral weight, we find an increase of $\theta_K$ that peaks at $\approx$100 fs and is followed by a subsequent decrease. Second, at the $\Sigma$ valley, we observe that $\theta_\Sigma$ is nearly constant up to delays of $\approx$100 fs before it decreases and saturates on a longer timescale. These observations can now directly be connected to the formation dynamics of dark NEQ excitonic occupations and their subsequent thermalization: For $\Delta t \approx 0$ fs, $KK$ excitons are optically excited and the small $\boldsymbol{Q}$-momentum width translates to a comparably small

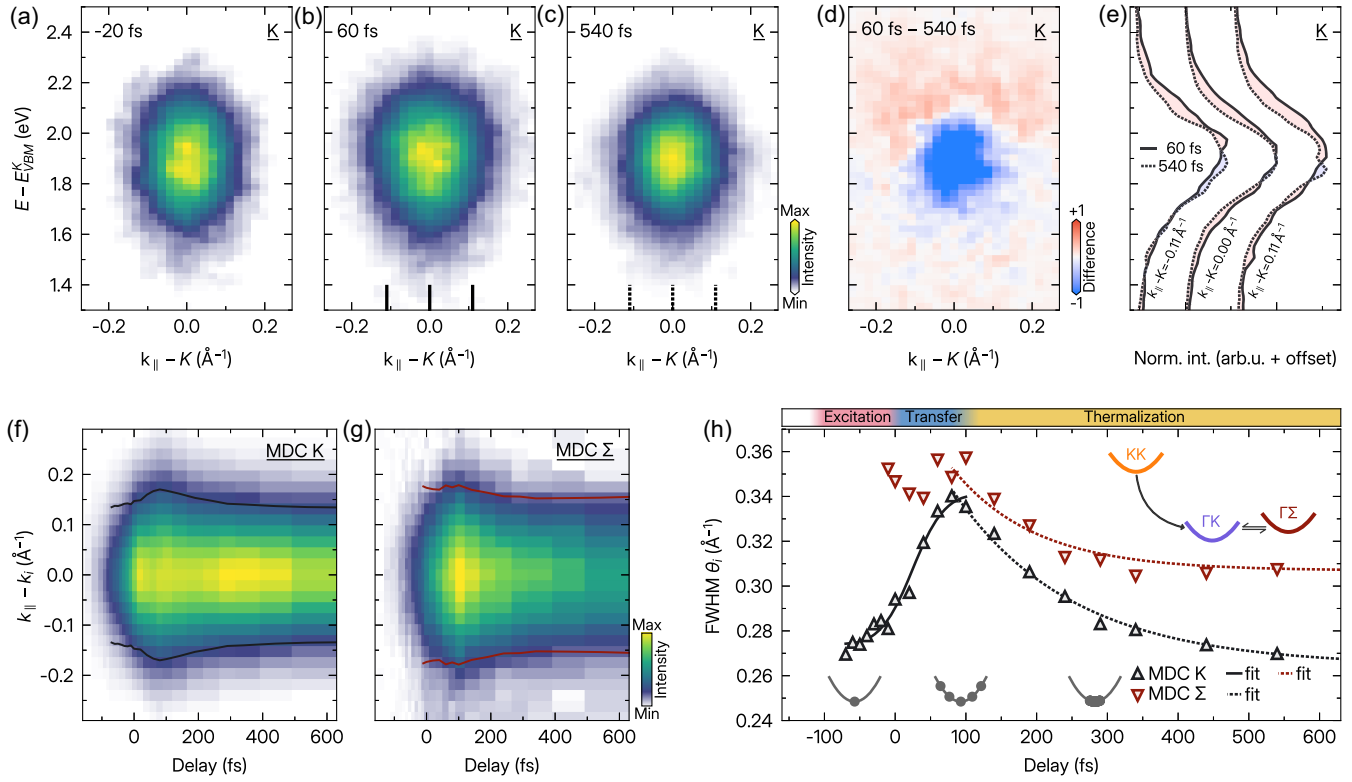


FIG. 4. Fingerprints for NEQ and thermalized exciton populations. (a)–(c) Photoemission snapshots taken at the $K$ valley at −20, 60, and 540 fs, respectively. (d),(e) Difference map of the 60 and 540 fs measurement (d) and momentum-filtered energy-distribution curves (e). (f),(g) Delay-dependent change of energy-integrated MDCs filtered at the $K$ valley (f) and the Σ valley (g) (energy-integration range: 1.5 − 2.4 eV). The solid lines indicate the FWHM $\theta_K$ and $\theta_\Sigma$ as extracted by fitting the MDCs with Gaussian distributions (see End Matter). (h) $\theta_K$ (black triangles) and $\theta_\Sigma$ (brown triangles) as a function of delay. The gray parabolas and dots illustrate the contribution of $\boldsymbol{Q} \approx 0$ excitons during optical excitation ($-100$ fs $< \Delta t < 0$ fs, red delay regime), the formation of $\boldsymbol{Q} \neq 0$ excitonic occupations due to exciton-phonon scattering (0 fs $< \Delta t <$ 100 fs, blue), and the subsequent thermalization toward $\boldsymbol{Q} \approx 0$ ($\Delta t >$ 100 fs, yellow). The solid and dotted lines are fits to the data, as summarized in Table II in End Matter.

$\theta_K$ value [39]. For increasing delay, $\theta_K$ is expected to increase for two reasons: First, photoelectrons with slightly larger $\boldsymbol{k}_\parallel$ are detected because of intravalley exciton-phonon scattering that induces a comparably small $\boldsymbol{Q} > 0$ $KK$ distribution [Figs. 3(b) and 3(c)]. Second, intervalley hole transfer leads to a $\boldsymbol{Q} > 0$ $\Gamma K$ exciton population that must strongly contribute to the measured broadening at $K$ [cf. Fig. 3(c)].

In addition to the NEQ exciton population dynamics in the $KK$ and $\Gamma K$ states, we can also analyze the formation and thermalization dynamics of the NEQ exciton population in the ΓΣ state. Since exciton-phonon scattering leads to a NEQ ΓΣ exciton occupation, we expect to find a broad momentum distribution that gradually sharpens with time. Indeed, for delays as early as the signal-to-noise ratio allows one to extract $\theta_\Sigma$, we find that $\theta_\Sigma$ is already at $\theta_\Sigma(0\ \text{fs}) \approx 0.35\ \text{Å}^{-1}$, while the signal in the $K$ valley is narrower with $\theta_K(0\ \text{fs}) \approx 0.29\ \text{Å}^{-1}$. This observation aligns with the theoretical model, which predicts that the ΓΣ population initially forms in a NEQ distribution.

On the longer timescale, both NEQ exciton populations at $\Gamma K$ and ΓΣ are expected to thermalize via additional exciton-phonon scattering events that dissipate excess energy. Indeed, $\theta_K$ and $\theta_\Sigma$ decrease on timescales $> 100$ fs with decay constants of $\tau = (170 \pm 15)$ fs and $\tau = (120 \pm 30)$ fs, respectively [Fig. 4(h), dotted lines]. Interestingly, the similar dynamics of the narrowing of the $K$- and Σ-valley MDC width supports the theoretical prediction that not only intravalley exciton-phonon scattering thermalizes the NEQ distributions, but that phonon emission events mediate efficient intervalley electron-transfer between $\Gamma K$ and ΓΣ excitons. Hence, the excitonic occupation jointly thermalizes toward a $\Gamma K \rightleftharpoons \Gamma\Sigma$ steady state.

*Discussion and outlook*—We have shown that the time-, energy-, and $\boldsymbol{k}_\parallel$-momentum-resolved photoemission experiment provides access not only to bright and dark excitons, but, by analyzing the delay-dependent evolution of the photoelectron $\boldsymbol{k}_\parallel$-momentum width, also to the energy- and $\boldsymbol{Q}$-momentum-resolved NEQ exciton population dynamics. Specifically, in BL 2H-$MoS_2$, we have illustrated

that we can directly access the formation dynamics of a NEQ exciton population of momentum-indirect $\Gamma K$ and $\Gamma\Sigma$ excitons that subsequently thermalize to a $\Gamma K \rightleftharpoons \Gamma\Sigma$ steady state. More broadly, our Letter shows how momentum microscopy gives experimental access to the $\boldsymbol{Q}$-momentum-resolved dynamics of excitons. Therewith, it will be possible to study the impact of other $\boldsymbol{Q}$-momentum-conserving scattering mechanisms such as Auger recombination [27] and exchange scattering [16,33]. Moreover, we emphasize that such direct access to NEQ exciton dynamics is important for the study of emergent moiré-trapped exciton states [9–11,32] and for access to even more complex quasiparticles such as self-hybridized exciton polaritons [63] or even exciton-polariton condensates [64].

*Acknowledgments*—This work was funded by the Deutsche Forschungsgemeinschaft (DFG, German Research Foundation)—432680300/SFB 1456 (Project No. B01), 217133147/SFB 1073 (Projects No. B07 and No. B10), 223848855/SFB 1083 (Project No. B9), the Priority Program SPP 2244 "2DMP" (Project No. 535247173), and the individual research Grants No. 542873258 and No. 571553489. E. M. and M. R. acknowledge funding from LOEWE-Exploration (HMWK Hesse). A. A. and S. H. acknowledge funding from EPSRC (EP/T001038/1, EP/P005152/1). A. A. acknowledges financial support by the Saudi Arabian Ministry of Higher Education. K. W. and T. T. acknowledge support from the JSPS KAKENHI (Grants No. 21H05233 and No. 23H02052), the CREST (JPMJCR24A5), JST, and World Premier International Research Center Initiative (WPI), MEXT, Japan. We acknowledge David Urbaniak for help with AFM imaging.

J. L., D. St., S. H., R. T. W., E. M., G. S. M. J., S. M., and M. R. conceived the research. P. W., A. A., and A. S. fabricated the samples. P. W., W. B., J. P. B., D. S., and M. M. carried out the time-resolved momentum microscopy experiments. P. W. analyzed the experimental data and prepared the figures. G. M. carried out the theoretical calculations guided by E. M. All authors discussed the results. S. M. and M. R. wrote the manuscript with contributions from all coauthors. K. W. and T. T. synthesized the hBN crystals.

*Data availability*—The data that support the findings of this article are openly available [65].

[1] S.-J. Liang, B. Cheng, X. Cui, and F. Miao, Van der Waals heterostructures for high-performance device applications: Challenges and opportunities, Adv. Mater. **32**, 1903800 (2020).

[2] T. Mueller and E. Malic, Exciton physics and device application of two-dimensional transition metal dichalcogenide semiconductors, npj 2D Mater. Appl. **2**, 29 (2018).

[3] G. Wang, A. Chernikov, M. M. Glazov, T. F. Heinz, X. Marie, T. Amand, and B. Urbaszek, Colloquium: Excitons in atomically thin transition metal dichalcogenides, Rev. Mod. Phys. **90**, 021001 (2018).

[4] R. Perea-Causin, D. Erkensten, J. M. Fitzgerald, J. J. P. Thompson, R. Rosati, S. Brem, and E. Malic, Exciton optics, dynamics, and transport in atomically thin semiconductors, APL Mater. **10**, 100701 (2022).

[5] D. A. Ruiz-Tijerina and V. I. Fal'ko, Interlayer hybridization and moiré superlattice minibands for electrons and excitons in heterobilayers of transition-metal dichalcogenides, Phys. Rev. B **99**, 125424 (2019).

[6] Y. Wang, Z. Wang, W. Yao, G.-B. Liu, and H. Yu, Interlayer coupling in commensurate and incommensurate bilayer structures of transition-metal dichalcogenides, Phys. Rev. B **95**, 115429 (2017).

[7] A. Chernikov, A. M. van der Zande, H. M. Hill, A. F. Rigosi, A. Velauthapillai, J. Hone, and T. F. Heinz, Electrical tuning of exciton binding energies in monolayer $WS_2$, Phys. Rev. Lett. **115**, 126802 (2015).

[8] A. Raja, A. Chaves, J. Yu, G. Arefe, H. M. Hill, A. F. Rigosi, T. C. Berkelbach, P. Nagler, C. Schüller, T. Korn, C. Nuckolls, J. Hone, L. E. Brus, T. F. Heinz, D. R. Reichman, and A. Chernikov, Coulomb engineering of the bandgap and excitons in two-dimensional materials, Nat. Commun. **8**, 15251 (2017).

[9] E. M. Alexeev, D. A. Ruiz-Tijerina, M. Danovich, M. J. Hamer, D. J. Terry, P. K. Nayak, S. Ahn, S. Pak, J. Lee, J. I. Sohn, M. R. Molas, M. Koperski, K. Watanabe, T. Taniguchi, K. S. Novoselov, R. V. Gorbachev, H. S. Shin, V. I. Fal'ko, and A. I. Tartakovskii, Resonantly hybridized excitons in moiré superlattices in van der Waals heterostructures, Nature (London) **567**, 81 (2019).

[10] K. Tran *et al.*, Evidence for moiré excitons in van der Waals heterostructures, Nature (London) **567**, 71 (2019).

[11] K. L. Seyler, P. Rivera, H. Yu, N. P. Wilson, E. L. Ray, D. G. Mandrus, J. Yan, W. Yao, and X. Xu, Signatures of moiré-trapped valley excitons in $MoSe_2/WSe_2$ heterobilayers, Nature (London) **567**, 66 (2019).

[12] Y. Xu, S. Liu, D. A. Rhodes, K. Watanabe, T. Taniguchi, J. Hone, V. Elser, K. F. Mak, and J. Shan, Correlated insulating states at fractional fillings of moiré superlattices, Nature (London) **587**, 214 (2020).

[13] C. Jin, E. Y. Ma, O. Karni, E. C. Regan, F. Wang, and T. F. Heinz, Ultrafast dynamics in van der Waals heterostructures, Nat. Nanotechnol. **13**, 994 (2018).

[14] X.-X. Zhang, Y. You, S. Y. F. Zhao, and T. F. Heinz, Experimental evidence for dark excitons in monolayer $WSe_2$, Phys. Rev. Lett. **115**, 257403 (2015).

[15] A. Raja, M. Selig, G. Berghäuser, J. Yu, H. M. Hill, A. F. Rigosi, L. E. Brus, A. Knorr, T. F. Heinz, E. Malic, and A. Chernikov, Enhancement of exciton–phonon scattering from monolayer to bilayer $WS_2$, Nano Lett. **18**, 6135 (2018).

[16] X. Jiang, Q. Zheng, Z. Lan, W. A. Saidi, X. Ren, and J. Zhao, Real-time GW-BSE investigations on spin-valley exciton dynamics in monolayer transition metal dichalcogenide, Sci. Adv. **7**, eabf3759 (2021).

[17] M. Selig, G. Berghäuser, M. Richter, R. Bratschitsch, A. Knorr, and E. Malic, Dark and bright exciton formation,

thermalization, and photoluminescence in monolayer transition metal dichalcogenides, 2D Mater. **5**, 035017 (2018).
[18] P. Merkl, F. Mooshammer, P. Steinleitner, A. Girnghuber, K. Q. Lin, P. Nagler, J. Holler, C. Schüller, J. M. Lupton, T. Korn, S. Ovesen, S. Brem, E. Malic, and R. Huber, Ultrafast transition between exciton phases in van der Waals heterostructures, Nat. Mater. **18**, 691 (2019).
[19] J. Madéo, M. K. L. Man, C. Sahoo, M. Campbell, V. Pareek, E. L. Wong, A. Al-Mahboob, N. S. Chan, A. Karmakar, B. M. K. Mariserla, X. Li, T. F. Heinz, T. Cao, and K. M. Dani, Directly visualizing the momentum-forbidden dark excitons and their dynamics in atomically thin semiconductors, Science **370**, 1199 (2020).
[20] R. Wallauer, R. Perea-Causin, L. Münster, S. Zajusch, S. Brem, J. Güdde, K. Tanimura, K.-Q. Lin, R. Huber, E. Malic, and U. Höfer, Momentum-resolved observation of exciton formation dynamics in monolayer $WS_2$, Nano Lett. **21**, 5867 (2021).
[21] J. P. Bange, P. Werner, D. Schmitt, W. Bennecke, G. Meneghini, A. AlMutairi, M. Merboldt, K. Watanabe, T. Taniguchi, S. Steil, D. Steil, R. T. Weitz, S. Hofmann, G. S. M. Jansen, S. Brem, E. Malic, M. Reutzel, and S. Mathias, Ultrafast dynamics of bright and dark excitons in monolayer $WSe_2$ and heterobilayer $WSe_2/MoS_2$, 2D Mater. **10**, 035039 (2023).
[22] F. Caruso, Nonequilibrium lattice dynamics in monolayer $MoS_2$, J. Phys. Chem. Lett. **12**, 1734 (2021).
[23] S. Ovesen, S. Brem, C. Linderälv, M. Kuisma, T. Korn, P. Erhart, M. Selig, and E. Malic, Interlayer exciton dynamics in van der Waals heterostructures, Commun. Phys. **2**, 23 (2019).
[24] G. Meneghini, M. Reutzel, S. Mathias, S. Brem, and E. Malic, Hybrid exciton signatures in ARPES spectra of van der Waals materials, ACS Photonics **10**, 3570 (2023).
[25] V. R. Policht, H. Mittenzwey, O. Dogadov, M. Katzer, A. Villa, Q. Li, B. Kaiser, A. M. Ross, F. Scotognella, X. Zhu, A. Knorr, M. Selig, G. Cerullo, and S. Dal Conte, Time-domain observation of interlayer exciton formation and thermalization in a $MoSe_2/WSe_2$ heterostructure, Nat. Commun. **14**, 7273 (2023).
[26] R. Rosati, K. Wagner, S. Brem, R. Perea-Causín, E. Wietek, J. Zipfel, J. D. Ziegler, M. Selig, T. Taniguchi, K. Watanabe, A. Knorr, A. Chernikov, and E. Malic, Temporal evolution of low-temperature phonon sidebands in transition metal dichalcogenides, ACS Photonics **7**, 2756 (2020).
[27] C. Poellmann, P. Steinleitner, U. Leierseder, P. Nagler, G. Plechinger, M. Porer, R. Bratschitsch, C. Schüller, T. Korn, and R. Huber, Resonant internal quantum transitions and femtosecond radiative decay of excitons in monolayer $WSe_2$, Nat. Mater. **14**, 889 (2015).
[28] M. Reutzel, G. S. M. Jansen, and S. Mathias, Probing excitons with time-resolved momentum microscopy, Adv. Phys. X **9**, 2378722 (2024).
[29] S. Dong, M. Puppin, T. Pincelli, S. Beaulieu, D. Christiansen, H. Hübener, C. W. Nicholson, R. P. Xian, M. Dendzik, Y. Deng, Y. W. Windsor, M. Selig, E. Malic, A. Rubio, A. Knorr, M. Wolf, L. Rettig, and R. Ernstorfer, Direct measurement of key exciton properties: Energy, dynamics, and spatial distribution of the wave function, Nat. Sci. **1**, e10010 (2021).
[30] M. K. L. Man, J. Madéo, C. Sahoo, K. Xie, M. Campbell, V. Pareek, A. Karmakar, E. L. Wong, A. Al-Mahboob, N. S. Chan, D. R. Bacon, X. Zhu, M. M. M. Abdelrasoul, X. Li, T. F. Heinz, F. H. da Jornada, T. Cao, and K. M. Dani, Experimental measurement of the intrinsic excitonic wave function, Sci. Adv. **7**, eabg0192 (2021).
[31] D. Schmitt, J. P. Bange, W. Bennecke, A. AlMutairi, G. Meneghini, K. Watanabe, T. Taniguchi, D. Steil, D. R. Luke, R. T. Weitz, S. Steil, G. S. M. Jansen, S. Brem, E. Malic, S. Hofmann, M. Reutzel, and S. Mathias, Formation of moiré interlayer excitons in space and time, Nature (London) **608**, 499 (2022).
[32] O. Karni *et al.*, Structure of the moiré exciton captured by imaging its electron and hole, Nature (London) **603**, 247 (2022).
[33] A. Kunin, S. Chernov, J. Bakalis, Z. Li, S. Cheng, Z. H. Withers, M. G. White, G. Schönhense, X. Du, R. K. Kawakami, and T. K. Allison, Momentum-resolved exciton coupling and valley polarization dynamics in monolayer $WS_2$, Phys. Rev. Lett. **130**, 046202 (2023).
[34] J. P. Bange, D. Schmitt, W. Bennecke, G. Meneghini, A. AlMutairi, K. Watanabe, T. Taniguchi, D. Steil, S. Steil, R. T. Weitz, G. S. M. Jansen, S. Hofmann, S. Brem, E. Malic, M. Reutzel, and S. Mathias, Probing electron-hole coulomb correlations in the exciton landscape of a twisted semiconductor heterostructure, Sci. Adv. **10**, eadi1323 (2024).
[35] D. Schmitt, J. P. Bange, W. Bennecke, G. Meneghini, A. AlMutairi, M. Merboldt, J. Pöhls, K. Watanabe, T. Taniguchi, S. Steil, D. Steil, R. T. Weitz, S. Hofmann, S. Brem, G. S. M. Jansen, E. Malic, S. Mathias, and M. Reutzel, Ultrafast nano-imaging of dark excitons, Nat. Photonics **19**, 187194 (2025).
[36] W. Bennecke, I. Gonzalez Oliva, J. P. Bange, P. Werner, D. Schmitt, M. Merboldt, A. M. Seiler, K. Watanabe, T. Taniguchi, D. Steil, R. T. Weitz, P. Puschnig, C. Draxl, G. S. M. Jansen, M. Reutzel, and S. Mathias, Hybrid Frenkel–Wannier excitons facilitate ultrafast energy transfer at a 2D–organic interface, Nat. Phys. **21**, 1973 (2025).
[37] E. Perfetto, D. Sangalli, A. Marini, and G. Stefanucci, First-principles approach to excitons in time-resolved and angle-resolved photoemission spectra, Phys. Rev. B **94**, 245303 (2016).
[38] A. Steinhoff, M. Florian, M. Rösner, G. Schönhoff, T. O. Wehling, and F. Jahnke, Exciton fission in monolayer transition metal dichalcogenide semiconductors, Nat. Commun. **8**, 1166 (2017).
[39] A. Rustagi and A. F. Kemper, Photoemission signature of excitons, Phys. Rev. B **97**, 235310 (2018).
[40] D. Christiansen, M. Selig, E. Malic, R. Ernstorfer, and A. Knorr, Theory of exciton dynamics in time-resolved ARPES: Intra- and intervalley scattering in two-dimensional semiconductors, Phys. Rev. B **100**, 205401 (2019).
[41] G. Meneghini, M. Löwe, R. Perea-Causin, J. P. Bange, W. Bennecke, M. Reutzel, S. Mathias, and E. Malic, ARPES signatures of trions in van der Waals materials, arXiv:2511.11448.
[42] K. F. Mak, C. Lee, J. Hone, J. Shan, and T. F. Heinz, Atomically thin $MoS_2$: A new direct-gap semiconductor, Phys. Rev. Lett. **105**, 136805 (2010).

[43] N. Scheuschner, O. Ochedowski, A.-M. Kaulitz, R. Gillen, M. Schleberger, and J. Maultzsch, Photoluminescence of freestanding single- and few-layer $MoS_2$, Phys. Rev. B **89**, 125406 (2014).
[44] M. Keunecke, C. Möller, D. Schmitt, H. Nolte, G. S. M. Jansen, M. Reutzel, M. Gutberlet, G. Halasi, D. Steil, S. Steil, and S. Mathias, Time-resolved momentum microscopy with a 1 MHz high-harmonic extreme ultraviolet beamline, Rev. Sci. Instrum. **91**, 063905 (2020).
[45] K. Medjanik, O. Fedchenko, S. Chernov, D. Kutnyakhov, M. Ellguth, A. Oelsner, B. Schönhense, T. R. F. Peixoto, P. Lutz, C.-H. Min, F. Reinert, S. Däster, Y. Acremann, J. Viefhaus, W. Wurth, H. J. Elmers, and G. Schönhense, Direct 3D mapping of the Fermi surface and Fermi velocity, Nat. Mater. **16**, 615 (2017).
[46] G. Meneghini, S. Brem, and E. Malic, Ultrafast phonon-driven charge transfer in van der Waals heterostructures, Nat. Sci. **2**, e20220014 (2022).
[47] I. C. Gerber, E. Courtade, S. Shree, C. Robert, T. Taniguchi, K. Watanabe, A. Balocchi, P. Renucci, D. Lagarde, X. Marie, and B. Urbaszek, Interlayer excitons in bilayer $MoS_2$ with strong oscillator strength up to room temperature, Phys. Rev. B **99**, 035443 (2019).
[48] I. Paradisanos, S. Shree, A. George, N. Leisgang, C. Robert, K. Watanabe, T. Taniguchi, R. J. Warburton, A. Turchanin, X. Marie, I. C. Gerber, and B. Urbaszek, Controlling interlayer excitons in $MoS_2$ layers grown by chemical vapor deposition, Nat. Commun. **11**, 2391 (2020).
[49] X. Zhu, D. R. Bacon, V. Pareek, J. Madéo, T. Taniguchi, K. Watanabe, M. K. L. Man, and K. M. Dani, A holistic view of the dynamics of long-lived valley polarized dark excitonic states in monolayer $WS_2$, Nat. Commun. **16**, 6385 (2025).
[50] S. Kusaba, K. Watanabe, T. Taniguchi, K. Yanagi, and K. Tanaka, Role of dark exciton states in the relaxation dynamics of bright 1s excitons in monolayer $WSe_2$, Appl. Phys. Lett. **119**, 093101 (2021).
[51] Z. Jin, X. Li, J. T. Mullen, and K. W. Kim, Intrinsic transport properties of electrons and holes in monolayer transition-metal dichalcogenides, Phys. Rev. B **90**, 045422 (2014).
[52] W. Jin, P.-C. Yeh, N. Zaki, D. Zhang, J. T. Sadowski, A. Al-Mahboob, A. M. van der Zande, D. A. Chenet, J. I. Dadap, I. P. Herman, P. Sutter, J. Hone, and R. M. Osgood, Direct measurement of the thickness-dependent electronic band structure of $MoS_2$ using angle-resolved photoemission spectroscopy, Phys. Rev. Lett. **111**, 106801 (2013).
[53] W. Bennecke, A. Windischbacher, D. Schmitt, J. P. Bange, R. Hemm, C. S. Kern, G. D'Avino, X. Blase, D. Steil, S. Steil, M. Aeschlimann, B. Stadtmüller, M. Reutzel, P. Puschnig, G. S. M. Jansen, and S. Mathias, Disentangling the multiorbital contributions of excitons by photoemission exciton tomography, Nat. Commun. **15**, 1804 (2024).
[54] See Supplemental Material at http://link.aps.org/supplemental/10.1103/w29j-z48v for a description of the theoretical modeling, which includes Refs. [55–62].
[55] S. Brem, K.-Q. Lin, R. Gillen, J. M. Bauer, J. Maultzsch, J. M. Lupton, and E. Malic, Hybridized intervalley moiré excitons and flat bands in twisted $WSe_2$ bilayers, Nanoscale **12**, 11088 (2020).
[56] J. Hagel, S. Brem, C. Linderälv, P. Erhart, and E. Malic, Exciton landscape in van der Waals heterostructures, Phys. Rev. Res. **3**, 043217 (2021).
[57] S. Brem, M. Selig, G. Berghaeuser, and E. Malic, Exciton relaxation cascade in two-dimensional transition metal dichalcogenides, Sci. Rep. **8**, 8238 (2018).
[58] G. Meneghini, S. Brem, and E. Malic, Ultrafast phonon-driven charge transfer in van der Waals heterostructures, Nat. Sci. **2**, e20220014 (2022).
[59] Z. Jin, X. Li, J. T. Mullen, and K. W. Kim, Intrinsic transport properties of electrons and holes in monolayer transition-metal dichalcogenides, Phys. Rev. B **90**, 045422 (2014).
[60] M. Kira and S. W. Koch, Many-body correlations and excitonic effects in semiconductor spectroscopy, Prog. Quantum Electron. **30**, 155 (2006).
[61] H. Haug and S. W. Koch, *Quantum Theory of the Optical and Electronic Properties of Semiconductors* (World Scientific, Singapore, 2009).
[62] E. Malic and A. Knorr, *Graphene and Carbon Nanotubes: Ultrafast Optics and Relaxation Dynamics* (John Wiley & Sons, New York, 2013).
[63] Z. Fei, M. E. Scott, D. J. Gosztola, J. J. Foley, J. Yan, D. G. Mandrus, H. Wen, P. Zhou, D. W. Zhang, Y. Sun, J. R. Guest, S. K. Gray, W. Bao, G. P. Wiederrecht, and X. Xu, Nano-optical imaging of $WSe_2$ waveguide modes revealing light-exciton interactions, Phys. Rev. B **94**, 081402(R) (2016).
[64] T. Byrnes, N. Y. Kim, and Y. Yamamoto, Exciton–polariton condensates, Nat. Phys. **10**, 803 (2014).
[65] P. Werner, W. Bennecke, J. P. Bange, G. Meneghini, D. Schmitt, M. Merboldt, A. M. Seiler, A. AlMutairi, K. Watanabe, T. Taniguchi, G. S. M. Jansen, J. Liu, D. Steil, S. Hofmann, R. T. Weitz, E. Malic, S. Mathias, and M. Reutzel, Replication data for: The role of non-equilibrium populations in dark exciton formation (2026), 10.25625/EKTPZZ.
[66] A. M. Seiler, Y. Zhumagulov, K. Zollner, C. Yoon, D. Urbaniak, F. R. Geisenhof, K. Watanabe, T. Taniguchi, J. Fabian, F. Zhang, and R. T. Weitz, Layer-selective spin-orbit coupling and strong correlation in bilayer graphene, 2D Mater. **12**, 035009 (2025).
[67] M. Düvel, M. Merboldt, J. P. Bange, H. Strauch, M. Stellbrink, K. Pierz, H. W. Schumacher, D. Momeni, D. Steil, G. S. M. Jansen, S. Steil, D. Novko, S. Mathias, and M. Reutzel, Far-from-equilibrium electron–phonon interactions in optically excited graphene, Nano Lett. **22**, 4897 (2022).
[68] M. Merboldt, M. Schüler, D. Schmitt, J. P. Bange, W. Bennecke, K. Gadge, K. Pierz, H. W. Schumacher, D. Momeni, D. Steil, S. R. Manmana, M. A. Sentef, M. Reutzel, and S. Mathias, Observation of Floquet states in graphene, Nat. Phys. **21**, 10931099 (2025).
[69] L. Miaja-Avila, C. Lei, M. Aeschlimann, J. L. Gland, M. M. Murnane, H. C. Kapteyn, and G. Saathoff, Laser-assisted photoelectric effect from surfaces, Phys. Rev. Lett. **97**, 113604 (2006).
[70] B. Schönhense, K. Medjanik, O. Fedchenko, S. Chernov, M. Ellguth, D. Vasilyev, A. Oelsner, J. Viefhaus, D. Kutnyakhov, W. Wurth, H. J. Elmers, and G. Schönhense, Multidimensional photoemission spectroscopy—The space-charge limit, New J. Phys. **20**, 033004 (2018).

[71] F. Roth, J. Mahl, M. Borgwardt, L. Wenthaus, F. Brausse, V. Garbe, O. Gessner, and W. Eberhardt, Dynamical nonlinear inversion of the surface photovoltage at Si(100), Phys. Rev. Lett. **132**, 146201 (2024).
[72] Y. Li, A. Chernikov, X. Zhang, A. Rigosi, H. M. Hill, A. M. van der Zande, D. A. Chenet, E.-M. Shih, J. Hone, and T. F. Heinz, Measurement of the optical dielectric function of monolayer transition-metal dichalcogenides: $MoS_2$, $MoSe_2$, $WS_2$, and $WSe_2$, Phys. Rev. B **90**, 205422 (2014).
[73] M. Weinelt, M. Kutschera, T. Fauster, and M. Rohlfing, Dynamics of exciton formation at the Si(100) $c(4 \times 2)$ surface, Phys. Rev. Lett. **92**, 126801 (2004).

## End Matter

*Appendix A: Sample fabrication*—The sample was prepared by mechanically exfoliating a homobilayer of 2H-$MoS_2$ from a bulk crystal onto a polydimethylsiloxane substrate. The flake is placed on $36 \pm 1$-nm-thick hexagonal boron nitride [hBN; see Fig. 5(b)] on a niobium-doped strontiumtitanite substrate (Nb-STO, 0.1% doping) via dry-transfer stamping [66]. The bilayer nature of the sample is confirmed via optical contrast (see Fig. 7). A real space image of the sample acquired by photoemission electron microscopy is shown in Fig. 5(a) with the position of the aperture used for the ARPES measurements marked as a black dashed line. To prepare the sample for experiments, it is annealed at 670 K for 3 h under ultrahigh vacuum conditions. High sample quality is confirmed by the presence of clearly visible bands in the ARPES measurements with minimal background intensity.

*Appendix B: Femtosecond momentum microscopy*—A detailed description of the ultrafast momentum microscopy setup and its application to exfoliated van der Waals materials is provided in Refs. [44] and [31,34,35], respectively. In short, the multidimensional photoemission data are acquired with a time-of-flight momentum microscope (ToF-MM, Surface Concept GmbH) [45], and the extreme-ultraviolet light pulses (26.5 eV, 20 fs, *p*-polarized) are generated with a tabletop high harmonic generation beam line driven by a 300 W fiber laser (AFS Jena) operating at 500 kHz [44,67,68]. The pump light (1.9 eV, 40 fs, *s*-polarized, 3 $\mu J/cm^{-2}$ absorbed fluence, $9 \times 10^{12}$ $cm^{-2}$ exciton density) is generated by an optical parametric amplifier (Light Conversion).

In all experiments reported in the manuscript, we measure energy- and in-plane momentum-resolved photoemission data cubes for selected pump-probe delays. The cross-correlation of the pump and probe laser pulses is quantified to $75 \pm 5$ fs by evaluating the delay dependence of the laser-assisted photoelectric effect [68,69]. Before the data analysis, as detailed in Refs. [31,34], we correct the multidimensional data for space-charge and photovoltage effects [70,71].

*Appendix C: Estimation of exciton densities*—To determine the density of optically excited excitons in the sample, the absorbed fluence has to be estimated. The

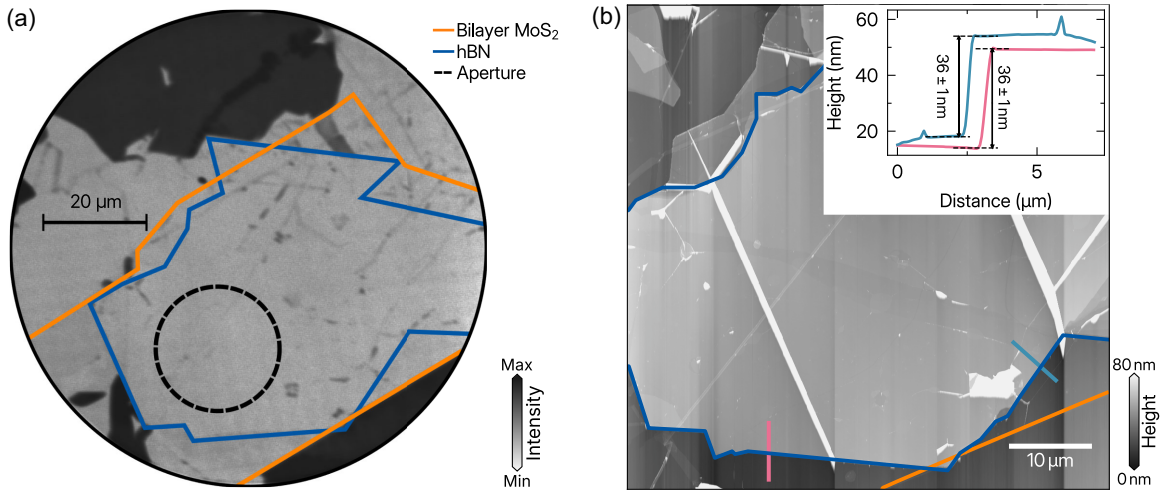


FIG. 5. Real space photoemission microscopy and atomic force microscopy (AFM) image of the 2H-$MoS_2$ homobilayer sample. (a) Image of the 2H-$MoS_2$ homobilayer flake using the photoemission electron microscopy mode of the momentum microscope. The black dashed circle marks the aperture position used for spatially selective momentum microscopy measurements. The orange polygon indicates the homobilayer 2H-$MoS_2$ flake; the blue outline marks the hBN buffer layer. Dark regions stem from the Nb-STO substrate. (b) AFM-image of the 2H-$MoS_2$ flake taken after all momentum microscopy experiments have been performed (blue polygon, hBN; orange polygon, 2H-$MoS_2$). The red and teal lines mark the extracted height profiles shown in the inset. The thickness of the hBN is determined to $36 \pm 1$ nm.

TABLE I. Low-energy landscape of excitons as extracted with trARPES, theory, and photoluminescence (PL) [42,43].

| Exciton | trARPES: $E^i_{\mathrm{exc}}$ (eV) | Theory: $E^i_{\mathrm{exc}}$ (eV) | PL (eV) [42,43] |
|---|---|---|---|
| $KK$ | $1.90 \pm 0.05$ | 1.89 | 1.88 |
| $K\Sigma$ | ⋯ | 1.98 | ⋯ |
| $\Gamma K$ | $1.52 \pm 0.05$ | 1.50 | 1.5 |
| $\Gamma\Sigma$ | $1.54 \pm 0.05$ | 1.55 | ⋯ |

spot size of the pump beam is determined in a real-space-resolved photoemission electron microscopy image to $215 \times 110\ \mu\mathrm{m}^2$. With the work function of the sample and the used photon energy (1.9 eV), photoemission occurs in nonlinear order of three. Hence, the actual pump spot is larger by a factor of $\sqrt{3}$. With the incident pump power of 25 mW, we calculate the incident pump fluence 180 $\mu\mathrm{J/cm}^2$ (500 kHz repetition rate). Since the incident angle of the *s*-polarized pump photons is 22°, following Fresnel equations, 26.3% of the incident fluence is transmitted into the sample. A single monolayer $MoS_2$ absorbs 7.3% of the incident light flux for 1.9 eV photon energy [72]. Assuming that both layers absorb an equal amount of photons and using the substrate-dependent correction factor from Ref. [72] for the underlying hBN, the homobilayer absorbs approximately 6% of the transmitted fluence. This results in an exciton density of $9 \times 10^{12}\ \mathrm{cm}^{-2}$.

*Appendix D: Quantification of exciton energies $E^i_{\mathrm{exc}}$ with momentum microscopy*—Considering the conservation of energy and momentum during the breakup of excitons, momentum microscopy can facilitate the experimental characterization of the energy landscape of bright and dark excitons [28]. The energy $E_{\mathrm{elec}}$ of the measured single-particle photoelectron resulting from the breakup of excitons is given by $E_{\mathrm{elec}} = E_{\mathrm{hole}} + E^i_{\mathrm{exc}} + \hbar\omega$ ($\hbar\omega$: probe photon energy) [73]. Here, $E_{\mathrm{elec}}$ is referenced to the energy of the hole, $E_{\mathrm{hole}}$, and, therefore, to the corresponding VBM in the specific valley, where the former exciton's hole component resides after the breakup of the exciton by the photoemission process ($\hbar\omega$: probe photon energy). For example, for $\Gamma K$ excitons, this implies that $E^{\Gamma K}_{\mathrm{exc}}$ can be extracted by calculating the energy difference between the Γ-valley VBM and the *K*-valley exciton photoemission signal [Fig. 2(c)]. The experimentally quantified energy landscape of all contributing excitons is summarized in Table I and, importantly, shows an excellent agreement with the *ab initio* calculated exciton energies and earlier photoluminescence experiments [42,43].

*Appendix E: Quantification of the momentum width $\theta_i$ of the excitonic photoemission signal*—The energy- and center-of-mass momentum-resolved excitonic occupation is encoded in the in-plane momentum-resolved width of the photoemission intensity [39]. We quantify this in-plane momentum width $\theta_i$ for the *K*- and Σ-valley excitonic photoemission spectral weight as follows: First,

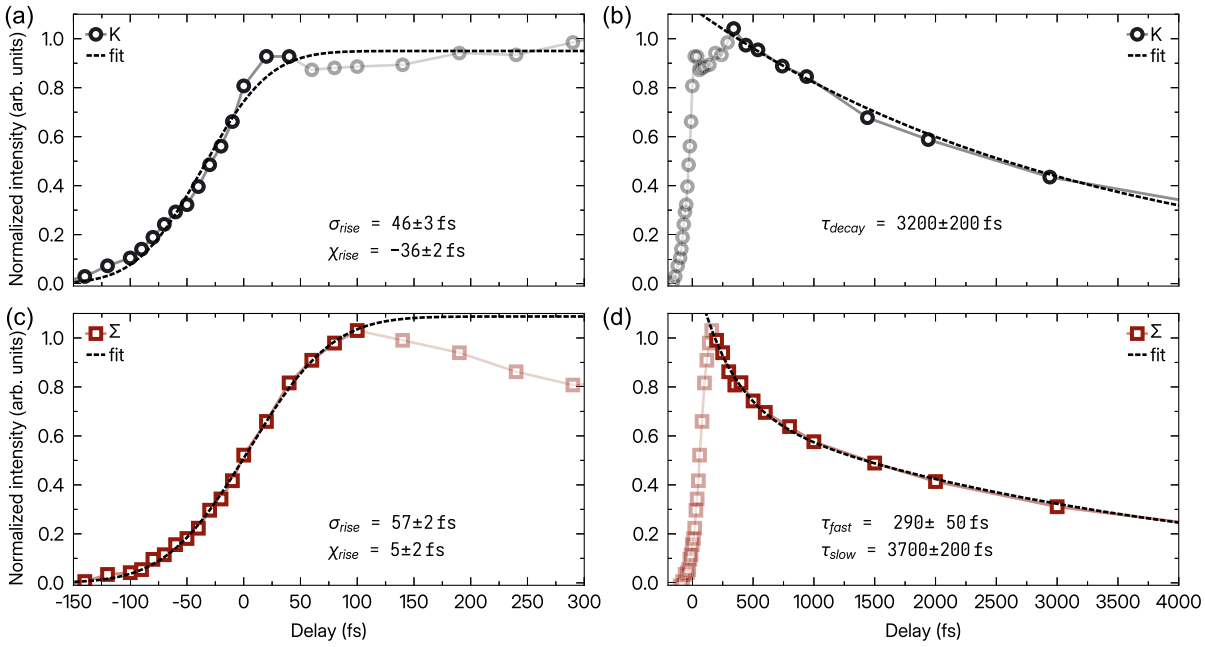


FIG. 6. Fit of rise and decay of excited state signal. (a) Rise of the excited state signal captured at the *K* valleys. (b) Single-exponential fit of the decay of the *K*-valley signal. (c) The same as (a) for the signal at the Σ valley. (d) Double-exponential fit of the decay of the Σ-valley signal. The fit results are summarized in Table II.

TABLE II. Overview of the fit results for the rise and decay of $K$- and Σ-valley excited state spectral weight, as well as the rise and decay of the momentum width $\theta_K$ and $\theta_\Sigma$. The fits are shown in Figs. 4(h) and 6.

| | $K$-valley intensity | Σ-valley intensity |
|---|---|---|
| $\sigma_{\text{rise}}$ (fs) | $46 \pm 3$ | $57 \pm 2$ |
| $\chi_{\text{rise}}$ (fs) | $-36 \pm 2$ | $5 \pm 2$ |
| $\tau_{\text{decay}}$ (fs) | $3200 \pm 200$ | ⋯ |
| $\tau_{\text{fast}}$ (fs) | ⋯ | $290 \pm 50$ |
| $\tau_{\text{slow}}$ (fs) | ⋯ | $3700 \pm 200$ |
| | $K$-valley FWHM | Σ-valley FWHM |
| $\sigma_{\text{rise},\theta}$ (fs) | $36 \pm 7$ | ⋯ |
| $\chi_{\text{rise},\theta}$ (fs) | $25 \pm 5$ | ⋯ |
| $\tau_{\text{decay},\theta}$ (fs) | $170 \pm 13$ | $120 \pm 30$ |

the $(k_x, k_y)$-momentum-resolved spectral weight is integrated in energy in a range from 1.5 to 2.4 eV for all six $K$ or Σ valleys. Second, the momentum maps are fitted with a 2D-Gaussian distribution with constant background.

*Appendix F: Quantification of the timescales for exciton formation, thermalization, and decay*—Table 2 summarizes the timescales for exciton formation, thermalization, and decay, as directly quantified from experiment. Thereby, we evaluate not only the photoemission spectral weight at the $K$ and the Σ valley, but also the momentum width $\theta_i$ $(i = K, \Sigma)$ of the excitonic photoemission signatures. The respective fits are shown in Figs. 4(h) and 6.

The rise time of the $K$- and Σ-valley spectral weight and also the rise time of the momentum width $\theta_K$ is fit with the error function

$$f = \frac{A}{2}\left[1 + \text{erf}\left(\frac{x-\chi}{\sqrt{2}\sigma}\right)\right]. \tag{F1}$$

Here, the fit parameters are the amplitude $A$, the position offset $\chi$, and the delay width $\sigma$. Note that the quantity referred to in the main text as rise time is the full width at half maximum of the error functions (i.e., $2.355\sigma$). The lifetime of the $K$- and Σ-valley spectral weight and also the decreasing momentum width $\theta_K$ and $\theta_\Sigma$ are fitted with single- or double-exponential functions of the form

$$f(x) = A\ \exp\left(-\frac{x-\chi}{\tau}\right) \tag{F2}$$

or

$$f(x) = A_1\ \exp\left(-\frac{x-\chi}{\tau_1}\right) + A_2\ \exp\left(-\frac{x-\chi}{\tau_2}\right). \tag{F3}$$

Here, the fit parameters are of two different amplitudes $A_1$ and $A_2$, timescales $\tau_1$ and $\tau_2$, and the delay offset $\chi$. The quantity referred to as thermalization timescale is the weighted mean of $\tau_{\text{decay},\theta}$ for the $K$- and Σ-valley momentum widths.

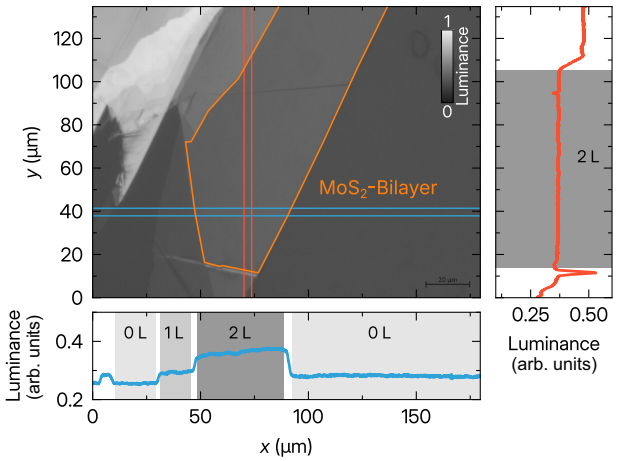


FIG. 7. Luminance map of the exfoliated $MoS_2$ flake. Luminance of an optical microscope image of the exfoliated $MoS_2$ bilayer. The optical density of $MoS_2$ varies with its layer thickness and, thus, allows for the determination of the number of layers. The main region of the flake outline by the orange line is a large bilayer region that was subsequently stamped on the hBN flake (see Fig. 5).